2014 22nd International Conference on Pattern Recognition

Automatic Liver Segmentation and Hepatic Fat Fraction Assessment in MRI

Zhennan Yan*, Chaowei Tan*, Shaoting Zhang†, Yan Zhou‡, Boubakeur Belaroussi§,
Hui Jing Yu§, Colin Miller§ and Dimitris Metaxas*
*CBIM, Rutgers University, Piscataway, USA 08854
†Department of Computer Science, University of North Carolina at Charlotte, Charlotte, USA 28223
‡Elekta Inc., Maryland Heights, USA 63043
§BioClinica Inc., Newtown, USA 18940 and Lyon, France 69008

***Abstract*—Automated assessment of hepatic fat fraction is clinically important. A robust and precise segmentation would enable accurate, objective and consistent measurement of liver fat fraction for disease quantification, therapy monitoring and drug development. However, segmenting the liver in clinical trials is a challenging task due to the variability of liver anatomy as well as the diverse sources the images were acquired from. In this paper, we propose an automated and robust framework for liver segmentation and assessment. It uses single statistical atlas registration to initialize a robust deformable model to get fine segmentation. Fat fraction map is computed by using chemical shift based method in the delineated region of liver. This proposed method is validated on 14 abdominal magnetic resonance (MR) volumetric scans. The qualitative and quantitative comparisons show that our proposed method can achieve better segmentation accuracy with less variance comparing with an automatic graph cut method. Experimental results demonstrate the promises of our assessment framework.**

***Keywords*—Segmentation; MRI; deformable model**

I. Introduction

Fatty liver, also known as hepatic steatosis, is a world-wide common condition characterized by fat accumulation in liver cells. It is associated with alcoholic liver disease, non-alcoholic fatty liver disease (NAFLD), drug toxicity and human immunodeficiency virus (HIV) [1]. The fatty liver is a reversible condition that may progress to more severe liver diseases. Therefore, the clinical diagnosis of fatty liver disease is important. This procedure often requires imaging studies, such as ultrasonography, X-ray computed tomography (CT), magnetic resonance imaging (MRI) and magnetic resonance spectroscopy (MRS). Previous studies have shown that the liver fat quantifications with MRI and MRS [2], [3], [4] are much better than ultrasonography and CT. Particularly, MRS is regarded as the most direct MR-based method to quantify water and fat components in liver. However, it is not widely applicable across standard clinical imaging centers due to the technical complexity. Instead, MRI based hepatic fat fraction measurement is widely used. It employs multi-echo chemical shift based methods and computes the fat fraction image voxel by voxel (sample images in Fig. 1). However, most studies only focus on improving the quantification of fat and water components, while the estimated fat fraction images are not liver specific. Doctors or clinical experts need to manually delineate regions of interest (ROI) and interpret the results in the whole MR images. Since 3D manual delineation of whole liver is low-efficient, high-cost and inconsistent, an automated and robust 3D liver segmentation is essential for quantitative measurements of hepatic fat fraction in clinical trials.

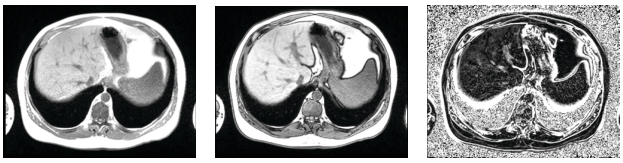

(a) In-phase (b) Out-of-phase (c) Fat fraction map

Fig. 1. Dual-phase MRI and fat fraction result.

In recent decades, there have been many automatic segmentation techniques proposed in medical image analysis. Usually, deformable model based methods [5], [6] are accurate but require good initializations. Atlas-guided approaches [7], [8], [9] assume the target has similar pathological and geometric characteristics with the training data. They require nonrigid registration [10] and some appearance dependent classification strategies [11] to segment the testing image. Many literatures and methods have been proposed for liver segmentation in CT images, including histogram based approach [12], shape constrained deformable model [13], graph cut [14], statistical atlas [15], and learning-based approaches [16], [17]. And several recent studies were done for MR images [18], [19]. However, most generative models are sensitive to data and initialization, while discriminative approaches usually require a large amount of training data with consistent imaging protocols, which may not be feasible in clinical trials and is label intensive. Besides, CT images have different appearance patterns with MR images which makes most algorithms designed for CT images not suitable for MRI's.

Robust liver segmentation in MRI is especially challenging for data sets in clinical trials, owing to their variety. Here we propose an automated and robust framework for liver segmentation. It only needs a small number of training data without constraining imaging protocols. Therefore, it is ideal for the hepatic fat fraction assessment in clinical trials. In our framework, a statistical image atlas is constructed and employed to obtain a rough estimation of liver ROI. Then, a robust deformable model is initialized from this estimation. Both edge and region information is used in this model for accurate and robust segmentation. The proposed segmentation

1051-4651/14 $31.00 © 2014 IEEE
DOI 10.1109/ICPR.2014.565

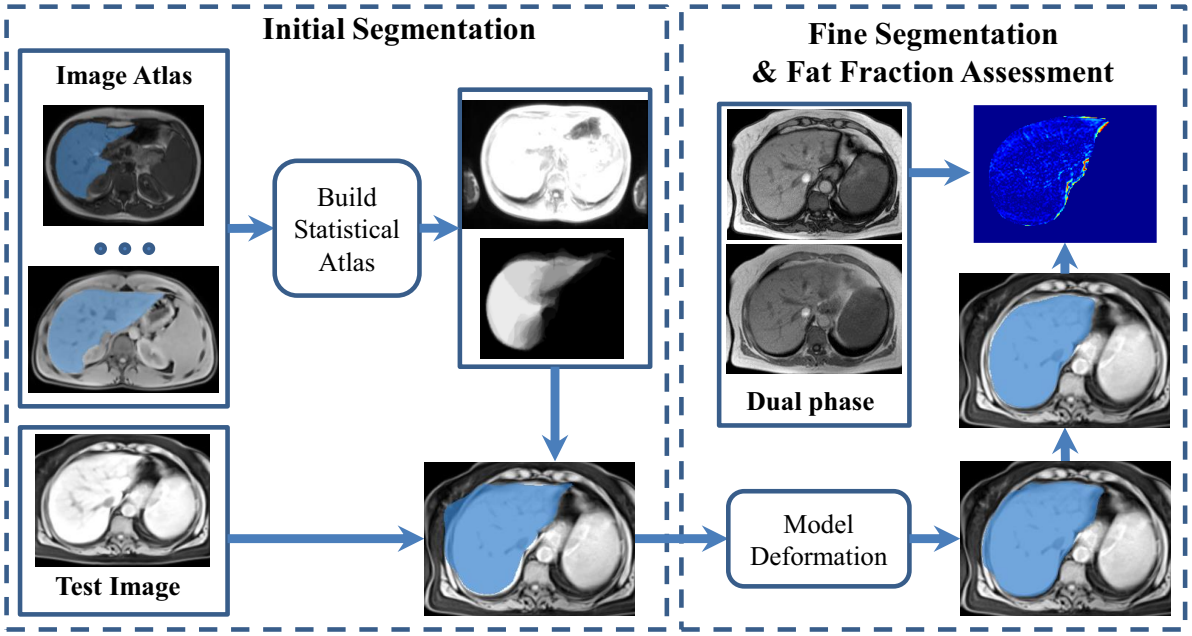

Fig. 2. Segmentation Framework.

method combines the reliability of atlas-based approach with the accuracy of deformable models. It is automatic and robust to segment liver from T1-weighted MRI. With the segmentation result, we can measure the fat fraction distribution in the liver region by magnitude based chemical shift method [2]. We evaluate this method on a data set of 14 volumetric MRI's from clinical trial. Our key contributions include the pipeline of the fatty liver analysis, and the segmentation algorithm using image atlas and deformable model.

II. Methodology

In this section, we introduce our framework for hepatic fat fraction assessment, including atlas-based initial segmentation and fine segmentation based on the robust deformable model (Fig. 2).

A. Initial Segmentation via Statistical Atlas

There usually exist some unknown noises and imaging artifacts in medical images, which can impact the accuracy of image analysis. Bias field is a low-frequency noise which can cause intensity inhomogeneities in MR images. Such inhomogeneities can make the object boundary ambiguous for segmentation algorithms. We use the improved nonparametric nonuniform intensity normalization (N4) method [20] to correct the bias field. A comparison between original T1 weighted MRI and bias corrected image is shown in Fig.3.

Given a small number of training images and their annotations, image atlas based approaches [11], [21] usually use appearance based label propagation techniques to segment an unseen target image. They perform well when segmenting new images with similar pathological and geometric characteristics as the atlas population (e.g. in normal-appearance brain segmentations) [22]. However, abdominal organs have large variant shapes, and some adjacent organs may have very similar intensities. So image atlas based approaches can hardly get an accurate segmentation of liver. On the other hand, this rough segmentation can be used as an initialization as demonstrated in [15].

In this work, we use a registration-based statistical atlas method to generate the initial segmentation. Let $\phi(\mathbf{x})\mathcal{I} = \mathcal{J}$ denote a transformation from source image $\mathcal{I}$ to target image $\mathcal{J}$ with nonrigid deformation field $\phi(\mathbf{x})$ after an affine registration, [23] proposed a symmetric diffeomorphic normalization (SyN) method which solves the problem to get $\phi(\mathbf{x})$ and inverse deformation field $\phi^{-1}(\mathbf{z})$ at the same time. Here, $\mathbf{x}, \mathbf{z}$ are spatial coordinates in D-dimensional images $\mathcal{I}$ and $\mathcal{J}$.

The mutual information (MI) and cross-correlation (CC) are two image similarity metrics commonly used in registration problems. MI estimates globally optimal matching between images, but may not be a good option in cases where non-stationary patterns require locally adaptive similarity measurement. On the other hand, CC depends only on local estimates and is suitable when locally varying intensities occur. To ensure the robustness of our framework to strong MRI inhomogeneity (bias field), we choose cross-correlation as the similarity metric in SyN method to do nonrigid registration. It is defined as Eq. 1, where $\mu_{\mathcal{I}_l}$ and $\mu_{\mathcal{J}_l}$ are local means in a n^D-sized window centered at each position $\mathbf{x}$ and $\mathbf{z}$; $\mathcal{I}_l$ and $\mathcal{J}_l$ are vector representations of image patches in the window.

$$CC(\mathcal{I}'_l, \mathcal{J}'_l) = \frac{(\mathcal{I}'_l \cdot \mathcal{J}'_l)^2}{(\mathcal{I}'_l \cdot \mathcal{I}'_l)(\mathcal{J}'_l \cdot \mathcal{J}'_l)} \tag{1a}$$

$$\mathcal{I}'_l = \mathcal{I}_l - \mu_{\mathcal{I}_l}, \quad \mathcal{J}'_l = \mathcal{J}_l - \mu_{\mathcal{J}_l} \tag{1b}$$

Given M training atlases, the statistical atlas is built following the algorithm 1. The $\mathcal{I}_i$ and $\mathcal{S}_i$ denote the training image

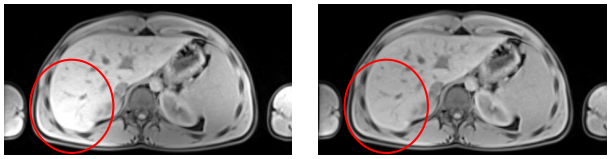

(a) Original T1 (b) Bias corrected

Fig. 3. Bias field correction results in axial view.

and its golden standard segmentation, respectively. In the output statistical atlas, $\bar{\mathcal{I}}$ is mean image and $\bar{\mathcal{S}}(\mathbf{x})$ represents probability of liver appearing at $\mathbf{x}$. In contrast to the Hounsfield unit scale in CT, the intensities of MRI data have various scales for the same tissue. To get the single reference image $\bar{\mathcal{I}}$ fused from training samples, we use the $Average$ function which normalizes the inputs individually before computing the average intensities at each voxel. Please note that since re-sampling is included in the transformation step, only $\mathcal{I}_m$ is re-sampled in line 2 and the warped $\hat{\mathcal{I}}_i$ also has isotropic $1mm$ voxel resolution in line 6. The motivation of the loop between line 3 and line 10 is to unbias the $\mathcal{I}_r$ which depends on the choice of m in the beginning. Here, we set the maximal iterations empirically as 2, thus $3M$ registrations are needed in total.

When a new target image comes, we compute transformation $\bar{\phi}_{\mathrm{T}}$ from $\bar{\mathcal{I}}$ to the target. Then the target-specific liver probability map $\bar{\mathcal{S}}_{\mathrm{T}} = \bar{\phi}_{\mathrm{T}}\bar{\mathcal{S}}$. An initial liver segmentation $\mathcal{S}_{\mathrm{Init}}$ is computed by thresholding $\mathcal{G}_\sigma * \bar{\mathcal{S}}_{\mathrm{T}}$ with a scalar value θ, where $\mathcal{G}_\sigma$ is a Gaussian smoothing filter with scale size σ.

B. Fine Segmentation via Deformable Model

This $\mathcal{S}_{\mathrm{Init}}$ is used as an initialization of a parametric active contour model, after converted to a high-quality surface mesh [24]. Starting from this initialization, deformable models [5], [6] can move through the spatial domain of an image under both internal (e.g. smoothness) and external (e.g. image) forces, and should converge to the desired object boundaries. However, these models may be sensitive to image noise, intensity inhomogeneity, and weak or misleading appearance cues. To ensure the robustness, our shape-based deformable model has the following energy terms:

$$E = E_{Int} + \kappa_1 \int_\Lambda [\mathcal{P}_E(\mathbf{x}) + \kappa_2 \mathcal{P}_R(\mathbf{x})] d\Lambda \qquad (2)$$

where E_{Int} is the traditional internal energy term constraining tension and rigidity. $\mathcal{P}_E(\mathbf{x}) = -\omega_e |\nabla \mathcal{G} * \mathcal{I}|^2$ is the image edge energy at $\mathbf{x}$, where $\nabla\mathcal{G}$ is a Gaussian derivative filter. $\mathcal{P}_R(\mathbf{x})$ is the image region energy defined like [25]. The object's interior intensity statistics provides important information to avoid the model stuck in the local minima and converge to the true object boundary. The combination of two external terms ensure that this model is robust to noise and ambiguous edges around liver. Here, κ_1, κ_2 and ω_e are all scalar values used as balances of different energy terms. We use the uniformly weighted Laplacian discrete representation [26] for the differential operators in internal energy term E_{Int}. Without re-meshing, the internal energy do not need to be evaluated in every iteration. The standard $\mathcal{P}_E(\mathbf{x})$ provides static external force from the input image which is also computed once

Algorithm 1 Build statistical atlas

Input:
The training atlases $\{\mathcal{I}_i, \mathcal{S}_i\}, i \in \{1, \ldots, M\}$;
Output:
The statistical atlas $\{\bar{\mathcal{I}}, \bar{\mathcal{S}}\}$;
1: pick an arbitrary m, where $m \in \{1, \ldots, M\}$
2: re-sample $\mathcal{I}_m$ to get $\mathcal{I}_r$ with isotropic $1mm$ voxel size
3: **while** $k < MAX\_ITERATION$ **do**
4: **for** $i = 1$ to M **do**
5: compute ϕ_i s.t. $\phi_i \mathcal{I}_r \approx \mathcal{I}_i$
6: $\hat{\mathcal{I}}_i = {\phi_i}^{-1} \mathcal{I}_i$
7: **end for**
8: $\mathcal{I}_r = Average(\{\hat{\mathcal{I}}_1, \cdots, \hat{\mathcal{I}}_M\})$
9: $k = k + 1$
10: **end while**
11: **for** $i = 1$ to M **do**
12: compute $\bar{\phi}_i$ s.t. $\bar{\phi}_i \mathcal{I}_r \approx \mathcal{I}_i$
13: $\hat{\mathcal{I}}_i = \bar{\phi}_i^{-1} \mathcal{I}_i$
14: $\hat{\mathcal{S}}_i = \bar{\phi}_i^{-1} \mathcal{S}_i$
15: **end for**
16: $\bar{\mathcal{I}} = Average(\{\hat{\mathcal{I}}_1, \cdots, \hat{\mathcal{I}}_M\})$
17: $\bar{\mathcal{S}} = \sum_{i=1}^{M} \hat{\mathcal{S}}_i / M$

before model evolution. Although the image region force in [25] is computed dynamically to enable larger capture range of Metamorphs deformable model, we only compute $\mathcal{P}_R(\mathbf{x})$ once in our work. We define the $\mathcal{P}_R(\mathbf{x}) = D^2$. The D is a distance map to the estimated object boundaries which maximizes the likelihood of pixel intensities inside current model surface. From our observations, the liver is a large organ in abdomen and the initial localization is reliable. Thus the liver intensity probability map can be computed once based on the initial liver distribution $\mathcal{G}_\sigma * \bar{\mathcal{S}}_{\mathrm{T}}$ and does not change a lot during iterations. Then the object boundary is estimated and the distance map D is computed. Since all the energy terms and corresponding forces are computed once at the beginning, our deformable model is efficient to converge.

The evolution of the deformable model is summarized as follows: 1) convert $\mathcal{S}_{\mathrm{Init}}$ to initial surface model $\mathbf{x}^{(0)}$; 2) compute initial and external forces; 3) deform model $\mathbf{x}^{(t-1)}$ to next time step $\mathbf{x}^{(t)}$; 4) smooth current model $\mathbf{x}^{(t)}$ in every 100 iterations; 5) repeat steps 3 to 4 until deformable model converges. Here, the step 4 is necessary because the mesh quality usually degenerates after iterations and may downgrade the final segmentation result. We choose a LowPass filter to do mesh smoothing which is recommended in [27].

C. Fat Fraction Assessment

For fat fraction assessment, we use dual-echo imaging based method [2], in which two series of images were acquired in a single breath-hold at two sequential echo times (TEs). At these two TEs, water and fat signals are out-of-phase (OP) and in-phase (IP), respectively. Then magnitude based chemical shift method is utilized to estimate the fat fraction (FF) map by: $FF = |S_{\mathrm{IP}} - S_{\mathrm{OP}}|/(2S_{\mathrm{IP}})$ [2], where S_{IP} and S_{OP} denote signals in IP and OP images. The range of fat fraction is limited to $0 - 50\%$ due to the absolute value in this method. Fortunately, it is acceptable in most cases since fat fractions greater than 50% are uncommon in liver [3].

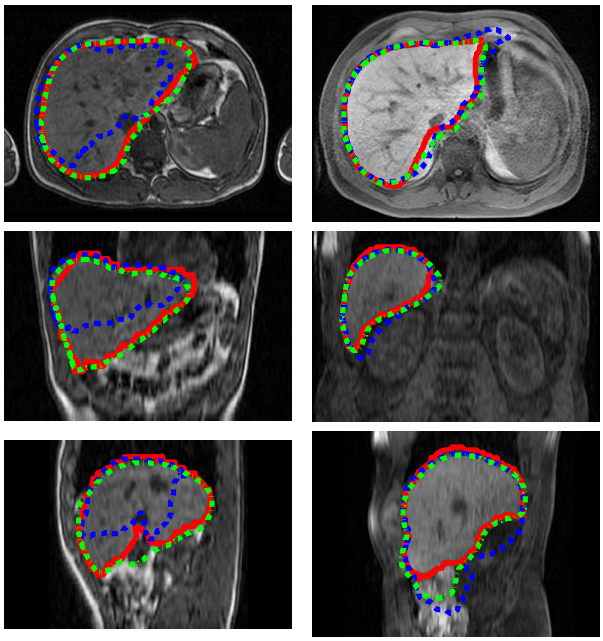

(a) Subject I (b) Subject II

Fig. 4. Comparison of initial (blue dotted line) and final (green dotted line) segmentation results against manual delineation (red solid line). First row is axial view; second row is coronal view; the last row is sagittal view.

III. EXPERIMENTS

In dual-echo imaging, OP and IP images are taken with a single breath-hold. The corresponding TEs are chosen as $2.3/4.6$ msec at 1.5T or $1.15/2.3$ msec at 3T. A database of 14 abdominal MR volumetric scans is used. Each subject has one pair of IP, OP scans and one T1-weighted MR scan. We choose T1-weighted MR images to segment liver, whose ground truths were manually labeled by experienced experts. Then we estimate hepatic fat fraction distribution using IP and OP images with segmented liver masks from T1 data. In our dataset, image resolutions of T1 MRI's range from 0.78 to 1.87mm in the axial slices with slice thickness from 3.5 to 7mm. The number of slices is from 30 to 104. The range in Z axis varies from 210mm to 364mm. The intensity is from 178 to 32767. We use 7 subjects as training set to train the statistical atlas and the rest 7 subjects as testing set.

We compare the proposed method with two other methods. One method is to use thresholding of the atlas registration result $\mathcal{S}_{\text{Init}}$ by a scalar θ to get a segmentation (denoted as Atlas). The other one is automatic graph cut method based on the probabilistic atlas initialization (denoted as Atlas+GC) [28]. We implemented the methods by our own. In Atlas+GC method, we assume 6-neighborhood connectivity, and the graph cut is solved by the min-cut/max-flow algorithm [29]. The region of interest is defined by the bounding box of $\mathcal{S}_{\text{Init}} > Th_{roi}$. The hard-constraint seeds of liver is set as those located in the region of $erode(\mathcal{S}_{\text{Init}} > Th_{liver})$, while the seeds of background is set as those outside of the region of $dilate(\mathcal{S}_{\text{Init}} > Th_{bg})$. All methods were implemented in Matlab, tested on 3.4 GHz Intel Core i7 computer with 8G RAM. We report the mean and variance values of the dice similarity coefficient ($\frac{2TP}{2TP+FP+FN}$), accuracy ($\frac{TP+TN}{TP+TN+FP+FN}$) and relative error ($\frac{FP+FN}{TP+FN}$) compared to the ground truth. TP, TN, FP and FN are number of voxels correctly identified, correctly rejected, incorrectly identified, and incorrectly rejected as liver tissue, respectively. We also measure the symmetrical surface distance error between the surfaces of segmentation results and those of the ground truth. Let X and Y denote point sets of ground truth surface mesh and segmentation result mesh, respectively; $p_X \in X$ is an arbitrary point in X. $\underset{X\to Y}{\mathrm{S}}(p_X)$ represents the point in Y which has the minimum Euclidean distance to p_X. $\underset{Y\to X}{\mathrm{S}'}(p_X)$ represents the point set in Y whose closest point in X is p_X. The symmetrical surface distance error at p_X is defined as the maximum Euclidean distance to $\{\underset{X\to Y}{\mathrm{S}}(p_X), \underset{Y\to X}{\mathrm{S}'}(p_X)\}$. In this error map, we can easily visualize and compare the surface error distribution of segmentation results referenced to the ground truth.

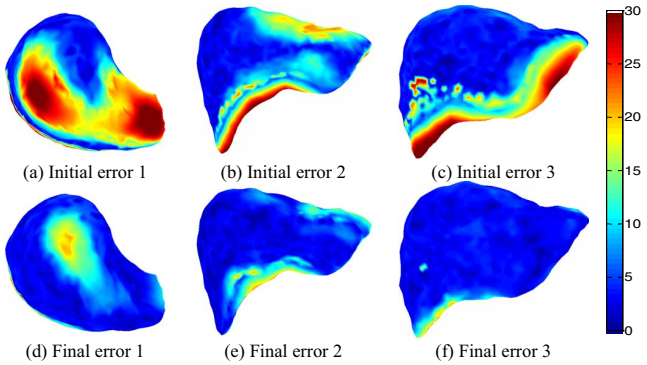

(a) Initial error 1 (b) Initial error 2 (c) Initial error 3

(d) Final error 1 (e) Final error 2 (f) Final error 3

Fig. 5. Comparison of surface distances to ground truth in three cases. First row is for initial segmentations; second row is for final segmentations.

As shown in Fig. 4, red lines are ground truth boundaries, blue lines are the initial segmentations, and the green lines are the final results from our proposed approach. It demonstrates that the deformable model refines the atlas-based segmentations to fit the real object boundary accurately. In Fig. 5, surface distances are plotted for three subjects in different view. Fig. 5.a-5.c show the surface distances between ground truth and initial segmentations, while Fig. 5.d-5.f show the surface errors of final segmentation results. The mean surface errors of the initial and final segmentations are $12.9mm$ and $7.4mm$, with standard deviations as 11.1 and 6.8, respectively. Quantitative comparisons of overlapping accuracies are shown in table I. The first row shows the segmentation results of $\mathcal{S}_{\text{Init}}$ with $\theta = 0.5$; the second row is from the proposed automatic graph cut method with $Th_{roi} = 0.1, Th_{liver} = 0.9, Th_{bg} = 0$; and the third row is from the proposed atlas+deformable model method.

Despite its inaccuracy, atlas-based method still provides good initializing for finer segmentations. The automatic graph cut approach has a larger variance and consumes huge memories during computation. Our proposed method has larger dice score and accuracy, as well as smaller relative error. It indicates that the proposed method has better average performance. Meanwhile the smaller standard deviations in last row show that it is more stable and robust comparing with the other

TABLE I. SEGMENTATION ACCURACY COMPARISON.

Method	Dice score		Accuracy		Relative error	
	μ	σ	μ	σ	μ	σ
Atlas	0.86	0.04	0.87	0.04	0.28	0.09
Atlas+GC	0.87	0.06	0.89	0.05	0.23	0.09
Ours	**0.90**	**0.02**	**0.91**	**0.02**	**0.20**	**0.05**

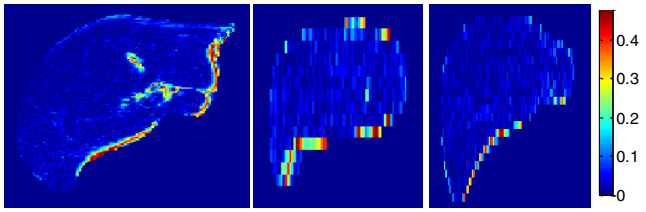

Fig. 6. Colored FFM in liver from different view (axial, sagittal and coronal).Values range from 0% to 50%.

two approaches. The parameters for deformable model was tuned for one subject and applied to all the testing subjects. In our implementation, $\kappa_1 = 1$, $\kappa_2 = 1$ and $\omega_e = 2.5$. The SyN registration is implemented in Advanced Normalization Tools (ANTs) [30]. We use CC metric with window radius 4, weight 1 and gradient step length 1.5. The optimization is performed on three resolutions with a maximum of 30 iterations at the coarsest level, 20 at the next coarsest and 10 at the full resolution, after the affine registration (200, 100, 50 maximal iterations respectively). We use a Gaussian regularizer with sigma of 3 that operates only on the similarity gradient and not on deformation field.

Finally, we transform the segmented liver masks from T1 image space to IP/OP image space by rigid registration. Fat fraction is assessed in liver region, where each voxel has a value indicating the ratio of fat component at that position. With the liver-specific FF distribution, it is easy to compute statistical measurements of fat ratio inside the liver tissue automatically. One assessment result is demonstrated in Fig. 6. For this subject, the mean fat fraction inside liver region is about 0.4%, while the maximum value is about 46% appearing along the liver boundary.

IV. CONCLUSION

We proposed a framework to segment 3D liver in MRI from clinical trials, followed by the assessment of the fat fraction map in the liver region. It utilizes image registration and trained statistical atlas to obtain a rough initialization, which is fed into robust deformable model for accurate segmentation. This statistical atlas not only provides a good initialization for the deformable model, but also is a reliable estimate of image region potential energy. The combination of these two modules enables efficient and accurate segmentation, from which the magnitude based chemical shift method computes the liver-specific fat fraction distribution. Our preliminary results demonstrate that this automatic system is robust to various liver shapes, different intensity distributions and low image resolution. In addition, it is an effective solution for clinical trials which have diverse data sources coming from different scanners and protocols. Our framework can be easily extended to segment other anatomies, as it does not require expensive training or prior knowledge. Since we only used observed feature in T1 weighted MRI, a potential improvement could be combination with in-phase and out-phase MRIs to get more comprehensive boundary features into the energy term of the deformable model for more accurate segmentation. Another possible enhancement could be incorporation of shape priors in the deformable model to further improve segmentation accuracy and efficiency. Sometimes the initial segmentation is relatively good and only sparse gross errors instead of Gaussian errors may be observed. In these cases, a sparse shape composite model [31], [32] can be incorporated into deformable model to refine the segmentation. Besides, the complex-based multi-echo fat assessment algorithm [3], [4] will be investigated. Unlike the magnitude-based approach we used, the complex-based approach permits a dynamic range of $0 - 100\%$ for fat-fraction, which could be a general solution to fat quantification of other tissues of interest, e.g. adipose, bone marrow, etc.

ACKNOWLEDGMENT

This project is partially funded by BioClinica Inc., NSF-MRI-1229628, and Center for Dynamic Data Analytics (NSF I/UCRC).

REFERENCES

[1] P. Angulo, "Nonalcoholic fatty liver disease," *New England Journal of Medicine*, vol. 346, no. 16, pp. 1221–1231, 2002.

[2] W. Dixon, "Simple proton spectroscopic imaging." *Radiology*, vol. 153, no. 1, pp. 189–194, 1984.

[3] S. Reeder, I. Cruite, G. Hamilton, and C. Sirlin, "Quantitative assessment of liver fat with magnetic resonance imaging and spectroscopy," *Journal of Magnetic Resonance Imaging*, vol. 34, no. 4, pp. 729–749, 2011.

[4] H. Yu, A. Shimakawa, C. Hines, C. McKenzie, G. Hamilton, C. Sirlin, J. Brittain, and S. Reeder, "Combination of complex-based and magnitude-based multiecho water-fat separation for accurate quantification of fat-fraction," *Magnetic Resonance in Medicine*, vol. 66, no. 1, pp. 199–206, 2011.

[5] M. Kass, A. Witkin, and D. Terzopoulos, "Snakes: Active contour models," *IJCV*, vol. 1, no. 4, pp. 321–331, 1988.

[6] C. Xu and J. L. Prince, "Snakes, shapes, and gradient vector flow," *IEEE Trans. Image Process.*, vol. 7, no. 3, pp. 359–369, 1998.

[7] J. Ashburner and K. Friston, "Unified segmentation," *NeuroImage*, vol. 26, pp. 839–851, 2005.

[8] T. Okada, R. Shimada, Y. Sato, M. Hori, K. Yokota, M. Nakamoto, Y.-W. Chen, H. Nakamura, and S. Tamura, "Automated segmentation of the liver from 3d ct images using probabilistic atlas and multi-level statistical shape model," in *Medical Image Computing and Computer-Assisted Intervention–MICCAI 2007*. Springer, 2007, pp. 86–93.

[9] X. Han, M. S. Hoogeman, P. C. Levendag, L. S. Hibbard, D. N. Teguh, P. Voet, A. C. Cowen, and T. K. Wolf, "Atlas-based auto-segmentation of head and neck CT images," in *Medical Image Computing and Computer-Assisted Intervention–MICCAI 2008*. Springer, 2008, pp. 434–441.

[10] X. Zhuang, K. S. Rhode, R. S. Razavi, D. J. Hawkes, and S. Ourselin, "A registration-based propagation framework for automatic whole heart segmentation of cardiac MRI," *Medical Imaging, IEEE Transactions on*, vol. 29, no. 9, pp. 1612–1625, 2010.

[11] K. Van Leemput, F. Maes, D. Vandermeulen, and P. Suetens, "Automated model-based tissue classification of MR images of the brain," *IEEE Trans. Med. Imag.*, vol. 18, no. 10, pp. 897–908, 1999.

[12] K.-S. Seo, "Improved fully automatic liver segmentation using histogram tail threshold algorithms," in *Computational Science–ICCS 2005*. Springer, 2005, pp. 822–825.

[13] D. Kainmüller, T. Lange, and H. Lamecker, "Shape constrained automatic segmentation of the liver based on a heuristic intensity model," in *Proc. MICCAI Workshop 3D Segmentation in the Clinic: A Grand Challenge*, 2007, pp. 109–116.

[14] L. Massoptier and S. Casciaro, "Fully automatic liver segmentation through graph-cut technique," in *EMBS*. IEEE, 2007, pp. 5243–5246.

[15] M. Linguraru, J. Sandberg, Z. Li, F. Shah, and R. Summers, "Automated segmentation and quantification of liver and spleen from CT images using normalized probabilistic atlases and enhancement estimation," *Medical physics*, vol. 37, pp. 771–783, 2010.

[16] H. Ling, S. Zhou, Y. Zheng, B. Georgescu, M. Suehling, and D. Comaniciu, "Hierarchical, learning-based automatic liver segmentation," in *CVPR*. IEEE, 2008, pp. 1–8.

[17] Y. Zhan, M. Dewan, and X. S. Zhou, "Cross modality deformable segmentation using hierarchical clustering and learning," in *Medical Image Computing and Computer-Assisted Intervention–MICCAI 2009*. Springer, 2009, pp. 1033–1041.

[18] R. Logeswaran, T. Haw, and S. Sarker, "Liver isolation in abdominal MRI," *Journal of medical systems*, vol. 32, no. 4, pp. 259–268, 2008.

[19] C. Platero, J. Poncela, P. Gonzalez, M. C. Tobar, J. Sanguino, G. Asensio, and E. Santos, "Liver segmentation for hepatic lesions detection and characterisation," in *ISBI*, 2008, pp. 13–16.

[20] N. J. Tustison, B. B. Avants, P. A. Cook, Y. Zheng, A. Egan, P. A. Yushkevich, and J. C. Gee, "N4itk: improved n3 bias correction," *IEEE Trans. Med. Imag.*, vol. 29, no. 6, pp. 1310–1320, 2010.

[21] S. Warfield, K. Zou, and W. Wells, "Simultaneous truth and performance level estimation (STAPLE): an algorithm for the validation of image segmentation," *IEEE Trans. Med. Imag.*, vol. 23, no. 7, pp. 903–921, 2004.

[22] Z. Yan, S. Zhang, X. Liu, D. N. Metaxas, and A. Montillo, "Accurate segmentation of brain images into 34 structures combining a non-stationary adaptive statistical atlas and a multi-atlas with applications to Alzheimer's disease," in *Biomedical Imaging (ISBI), 2013 IEEE 10th International Symposium on*. IEEE, 2013, pp. 1202–1205.

[23] B. Avants, C. Epstein, M. Grossman, and J. Gee, "Symmetric diffeomorphic image registration with cross-correlation: Evaluating automated labeling of elderly and neurodegenerative brain," *Medical image analysis*, vol. 12, no. 1, pp. 26–41, 2008.

[24] S. Zhang, Y. Zhan, X. Cui, M. Gao, J. Huang, and D. Metaxas, "3D anatomical shape atlas construction using mesh quality preserved deformable models," *Computer Vision and Image Understanding*, vol. 117, no. 9, pp. 1061 – 1071, 2013.

[25] X. Huang and D. N. Metaxas, "Metamorphs: deformable shape and appearance models," *IEEE Trans. Pattern Anal. Mach. Intell.*, vol. 30, no. 8, pp. 1444–1459, 2008.

[26] T. Shen, X. Huang, H. Li, E. Kim, S. Zhang, and J. Huang, "A 3D laplacian-driven parametric deformable model," in *Computer Vision (ICCV), 2011 IEEE International Conference on*. IEEE, 2011, pp. 279–286.

[27] R. Bade, J. Haase, and B. Preim, "Comparison of fundamental mesh smoothing algorithms for medical surface models," in *SimVis*, vol. 6. Citeseer, 2006, pp. 289–304.

[28] C. Platero, V. Rodrigo, M. C. Tobar, J. Sanguino, O. Velasco, and J. M. Poncela, "Probabilistic atlas based segmentation using affine moment descriptors and graph-cuts," in *Computer Analysis of Images and Patterns*. Springer, 2011, pp. 144–151.

[29] Y. Boykov and G. Funka-Lea, "Graph cuts and efficient nd image segmentation," *IJCV*, vol. 70, no. 2, pp. 109–131, 2006.

[30] B. B. Avants, N. Tustison, and G. Song, "Advanced normalization tools (ants)," *Insight J*, 2009.

[31] S. Zhang, Y. Zhan, M. Dewan, J. Huang, D. N. Metaxas, and X. S. Zhou, "Towards robust and effective shape modeling: Sparse shape composition," *Medical Image Analysis*, vol. 16, no. 1, pp. 265 – 277, 2012.

[32] S. Zhang, Y. Zhan, and D. N. Metaxas, "Deformable segmentation via sparse representation and dictionary learning," *Medical Image Analysis*, vol. 16, no. 7, pp. 1385–1396, 2012.